Microstructures and Grain Refinement of Additive-Manufactured Ti-xW Alloys

MICHAEL Y. MENDOZA, PEYMAN SAMIMI, DAVID A. BRICE,
BRIAN W. MARTIN, MATT R. ROLCHIGO, RICHARD LESAR,
and PETER C. COLLINS

It is necessary to better understand the composition–processing–microstructure relationships that exist for materials produced by additive manufacturing. To this end, Laser Engineered Net Shaping (LENS™), a type of additive manufacturing, was used to produce a compositionally graded titanium binary model alloy system (Ti-xW specimen ($0 \leq x \leq 30$ wt pct), so that relationships could be made between composition, processing, and the prior beta grain size. Importantly, the thermophysical properties of the Ti-xW, specifically its supercooling parameter (P) and growth restriction factor (Q), are such that grain refinement is expected and was observed. The systematic, combinatorial study of this binary system provides an opportunity to assess the mechanisms by which grain refinement occurs in Ti-based alloys in general, and for additive manufacturing in particular. The operating mechanisms that govern the relationship between composition and grain size are interpreted using a model originally developed for aluminum and magnesium alloys and subsequently applied for titanium alloys. The prior beta grain factor observed and the interpretations of their correlations indicate that tungsten is a good grain refiner and such models are valid to explain the grain-refinement process. By extension, other binary elements or higher order alloy systems with similar thermophysical properties should exhibit similar grain refinement.

I. INTRODUCTION

THE high level of interest in additive manufacturing (*i.e.*, 3D printing) has made it necessary to develop process–composition–microstructure and composition–microstructure–property relationships[1–3] for a variety of metallic alloys deposited using additive manufacturing techniques. This need, concurrently, has led to a number of research activities and publications on additive manufacturing, with common microstructural features observed, including (depending upon the processing parameters) large columnar grains,[4] compositional fluctuations,[3] unmelted particles or other anomalies,[5] zigzag grains,[6] and columnar-to-equiaxed transitions (CETs).[7] To develop the aforementioned relationships, it is necessary to understand at a minimum, and predict if possible, microstructural attributes including grain size, composition fluctuations, unmelted particles, grain orientation/crystal texture, and any spatial variations in these features. Once these initial attributes have been set, many of the subsequent phase transformations and microstructural configurations are governed (restricted).

Yet, there is a solution to this need. The additive manufacturing of metallic structures is fundamentally a melting and solidification problem, albeit one that often deviates from equilibrium processing and one for which composition may fluctuate from the intended composition. The fact that additive manufacturing is essentially a solidification problem at a small volume (0.2 mm^3 to 1 cm^3) means that there is an opportunity to use theories related to solidification to predict grain structures and sizes, as well as other microstructural attributes of interest (*e.g.*, texture). Additive manufacturing allows for a new exploration of alloy space where conventional processing may not be possible due to difficulties such as solute partitioning or macrosegregation in large ingots. Indeed, such alloys may be possible to process in a compositionally homogeneous manner by additive manufacturing. Some Ti-based alloys are prone to strong

MICHAEL Y. MENDOZA, DAVID A. BRICE, BRIAN W. MARTIN, and MATT R. ROLCHIGO are with the Department of Materials Science and Engineering, Iowa State University, Ames, IA, 50011. PEYMAN SAMIMI, RICHARD LESAR, and PETER C. COLLINS are with the Department of Materials Science and Engineering, Iowa State University, and also with the Center for Advanced Non-Ferrous Structural Alloys (CANFSA), a joint NSF I/UCRC between the Colorado School of Mines, Golden, CO, 80401, and Iowa State University. Contact e-mail:pcollins@iastate.edu

solute partitioning in the liquid, but are of general interest for additive manufacturing.

This paper explores both this need (*e.g.*, identifying models to predict grain size for additive manufacturing) and opportunity (*i.e.*, new alloy spaces) for grain refinement in titanium-based alloys. Further, it leverages a capability afforded by additive manufacturing to study more rapidly the effects of a single alloying element across a range of compositions—*i.e.*, a combinatorial approach. It also uses the concept of elemental powder blends.[8] Such an approach has intrinsic advantages as it allows multiple compositions to be affected in a single specimen that is subjected to nominally identical processing conditions and to determine the influence of composition on an attribute of interest. Such studies have been used in the past to study phase stability, composition–microstructure–property relationships, magnetic properties, and oxidation behavior.[9] Here, it is used to probe the fundamentals of composition on grain refinement. While the focus of this paper is on the effect of solute on grain refinement, necessarily, the work also investigates the effect of processing on homogeneity of elemental powder blends, correlated porosity, and grain size. It is important to note that one of the strong motivations to reduce the grain size in additive-manufactured materials is to influence the texture of the as-deposited material. Texture is pervasive in additively manufactured materials,[10] as the grains grow typically by epitaxial growth from the preexisting grains immediately under the molten pool. If nucleation events can be promoted in the molten pool, or the kinetics/thermodynamics of solidification modified, it may be possible to disrupt the native texture of additively manufactured metallic alloys.

Regarding grain refinement, typically, grain refinement of cast alloys can be attributed to: inoculants, other compositional effects, and cooling rate. When compositional effects are considered, more recent work investigates the role of two thermodynamic parameters, the supercooling parameter P and the growth restriction factor Q, expressed as Eqs. [1] and [2]:

$$P = \frac{mc_0(k-1)}{k} \qquad [1]$$

$$Q = mc_0(k-1) = \frac{\mathrm{d}\Delta T_c}{\mathrm{d}f_s} \qquad [2]$$

where m is the slope of the liquidus line and k is the partition coefficient.[11–15] In addition, the growth restriction factor is equivalent to the rate of development of constitutional undercooling (ΔT_c) relative to the rate of development of solid (f_s).[16] Recent work includes the work of Tamirisakandala *et al.* who reported the effect of boron on the grain refinement of as-cast Ti-6Al-4V and Ti-6242[17] and Bermingham *et al.* who studied the same effect for as-cast commercially pure titanium.[18] In these studies, an interpretation of the factor Q is that the boron solute is rejected in front of the solid-liquid interface, forming a boron rich undercooled region that restricts the growth of preexistent nuclei and necessarily increases the

probability to activate new nuclei. This interpretation has also been noted in a recent review paper by Collins *et al.* that[19] including side-by-side comparisons of the titanium alloy TNZT (nominally Ti-35Nb-7Zr-5Ta)[20] and a boron modified TNZT alloy,[21] where there was a potent grain-refinement effect upon the addition of boron.

Using a similar approach, Easton and St. John[22] developed a model for Al and Mg alloys to evaluate the grain refinement through a semi-empirical relationship that involves the contribution from the solute and the nuclei effects on grain size. The simplified equation is expressed in Eq. [3],

$$d = a + \frac{b}{Q} \qquad [3]$$

where d is the diameter of the grain, a is the y-intercept, defined by Eq. [4],

$$a = \frac{1}{(\rho \cdot f)^{1/3}} \qquad [4]$$

$$b = b_1 \Delta T_n \qquad [5]$$

where ρ is the density of nucleant particles and f is the activated fraction of particles, thus the a term is inversely proportional to the maximum number of activated nuclei. The term b is the slope defined in Eq. [5], where b_1 is a constant and ΔT_n is the undercooling necessary to activate nucleation. Higher values of b (the slope) represent lower potency of nuclei as they require a high undercooling (ΔT_n) to be activated.[13] Thus, b is inversely proportional to the potency of nuclei. Q is the previously defined growth restriction factor. Experimental results of Easton and St. John for Al alloys[22] and Mg alloys[23] showed that this relationship gave a good fit to the data. In a more recent research work conducted by Bermingham *et al.*,[24] the same model was applied to Ti refined by additions of silicon. The results were also in agreement with the Easton and St. John model, suggesting that the model is also applicable to Ti alloys.

To identify an alloying element that would be a suitable and strong grain refiner for Ti-based alloys, it is necessary to consider several aspects, including both the potential to refine the grain size and the supplemental effect for other properties. For example, while B and Si both have an ability to reduce the grain size,[17,25] these two elements will form intermetallic compounds that may have secondary (perhaps deleterious) effects on the microstructural evolution[24] or the mechanical properties[26] beyond a certain composition limit c_0. While the overall design of new alloy composition is well beyond this paper, multiple activities are underway[27] to provide tools that can be used in parallel with the emphasis of this paper—affecting grain size.

When considering grain size alone, it is clear that the growth restriction factor Q should be high to promote fine grain sizes. Several solute elements in small amounts with a high growth restriction factor Q have been evaluated in the past such as beryllium with the Q factor of $72C_0$,[12] Boron with the Q factor of $66C_0$[18] and

silicon with the Q factor of $21.7C_0$.[24] Tungsten is among the elements with a high Q factor of about $22.65C_0$, which has been largely neglected in the literature. These elements, as well as other potential binary systems,[12] are given in Table I. Generally, the Ti-W system is ignored due to two factors. Firstly, unmelted tungsten particles are the classic definition of high-density inclusions, for which advanced titanium melt practices have been designed to eliminate. Tungsten, in conventional melting, either doesn't melt, or results in strong solute partitioning and compositionally inhomogeneous structures. Secondly, W is dense, and will result in a non-trivial density increase of the alloy—reducing the technical advantages for aerospace applications. However, as noted above, it does have the potential to reduce the grain size, which may be of benefit in certain applications. In addition, W does not form intermetallic compounds, and is an isomorphous β-stabilizer, unlike B, Be, and Si (see Figures 1(a) through (d)). During additive manufacturing, strong solute partitioning will not operate to the same degree as conventional melt/ingot practices. However, even in an equilibrium system the parameters m and k are treated as constants independent of solute content C_0 (see Eq. [2]) and based upon an idealized system with straight transus boundaries.[28] Therefore, the implementation of these methods are an idealized approximation to additive manufacturing process, not dissimilar from an idealized approximation of casting. The results indicate that, to a first order, the approximations help explain several observations. In this study, the operating mechanism with regard to the grain-refinement effect of W has been explored as a model alloying element to Ti, across a wide compositional range, via a compositionally graded Ti-xW specimen ($0 \leq x \leq 30$ wt pct) which was produced using Laser Engineered Net Shaping (LENS™) technology.

II. EXPERIMENTAL PROCEDURE

A compositionally graded Ti-xW ($0 \leq x \leq 30$ wt pct) specimen was produced using an Optomec LENS™ 750 at the University of North Texas from high purity elemental metal powders of Ti (99.9 pct pure, −150

mesh from Alfa Aesar) and W (99.8 pct pure, plasma spray grade from Micron Metals). In this first AM system, the laser is a fixed optic Nd:YAG laser operating at 1064 nm provided by US Laser. The laser was operated between 350 and 500 W, and the atmosphere was kept below 20 ppm oxygen. In addition, a series of Ti-6 wt pct W alloys were deposited using an Optomec LENS™ system at Ames Laboratory. In this second AM system, the laser is a fiber optic Nd:YAG laser operating at 1064 nm provided by IPG. The IPG laser was operated between 183 and 367 W, and the atmosphere was kept below 5 ppm oxygen.

In both of these LENS™ systems, a computer-aided design (e.g. CAD) file is used in LENS™, from which a tool path is extracted for the subsequent laser deposition of a three dimensional specimen. The CAD file is converted and sliced into layers with a nominal thickness of 0.25 mm. Each layer consists of multiple parallel lines with a nominal hatch width of ~0.38 mm. The tool path that is generated based upon these variables is used to control the motorized stages (x,y) and a deposition head consist of focusing lens and powder nozzles mounted on the z motorized stage. The 2D (x,y) in-plane motion of the stage accompanied by −z vertical motion of the deposition head produce near-net-shape metallic pieces.

Two separate aspects of this research were conducted. The first research activity used the fixed-optic laser equipped with two powder feeders to assess the influence of W on the microstructure, in particular on the grain size. To conduct this first research activity, the LENS™ is equipped with two independently controlled powder feeders which were loaded with pure Ti powder in powder feeder #1 and with a Ti–30 wt pct W mechanically mixed elemental powder blend in powder feeder #2. An inert gas (here Ar) transports the powders from powder feeders into a controlled atmosphere box. The fluidized powders are injected (via four convergent Cu nozzles) into a localized melt pool created by a focused high-energy Nd:YAG laser and an energy density of 21.4 MJ/in^3 (~1305 kJ/cm^3). A 6-mm-thick Ti-6Al-4V substrate was used as the base for laser deposition of the powder blend and in situ alloying. The graded specimen deposit was a rectilinear solid of dimensions: 38 mm × 25 mm × 12 mm. The independent computer control of the powder flow rate allows for

Table I. Calculated Values for Several Elements in Titanium

Element	m_l	k	$Q = m_l (k − 1)*C_0$	$P = m_l (k − 1)*C_0/k$
Al	−2.1	→1	→$0C_0$	→$0C_0$
B	−66	→0	$66C_0$	$660C_0$
Be	−92	0.21	$72C_0$	$343C_0$
C	70	6.4	$378C_0$	$59C_0$
Cr	−8.1	0.81	1.54	$1.85C_0$
Cu	−10.6	0.39	$6.5C_0$	$16.6C_0$
Fe	−18	0.79	$3.8C_0$	$4.8C_0$
Mo	8.9	1.5	$4.5C_0$	$2.96C_0$
Nb	10	1.25	$2.5C_0$	$2C_0$
Si	−32.5	0.35	$21.7C_0$	$62C_0$
V	−4.7	→1	→$0C_0$	→$0C_0$
W	15.1	2.5	$22.65C_0$	$9.06C_0$

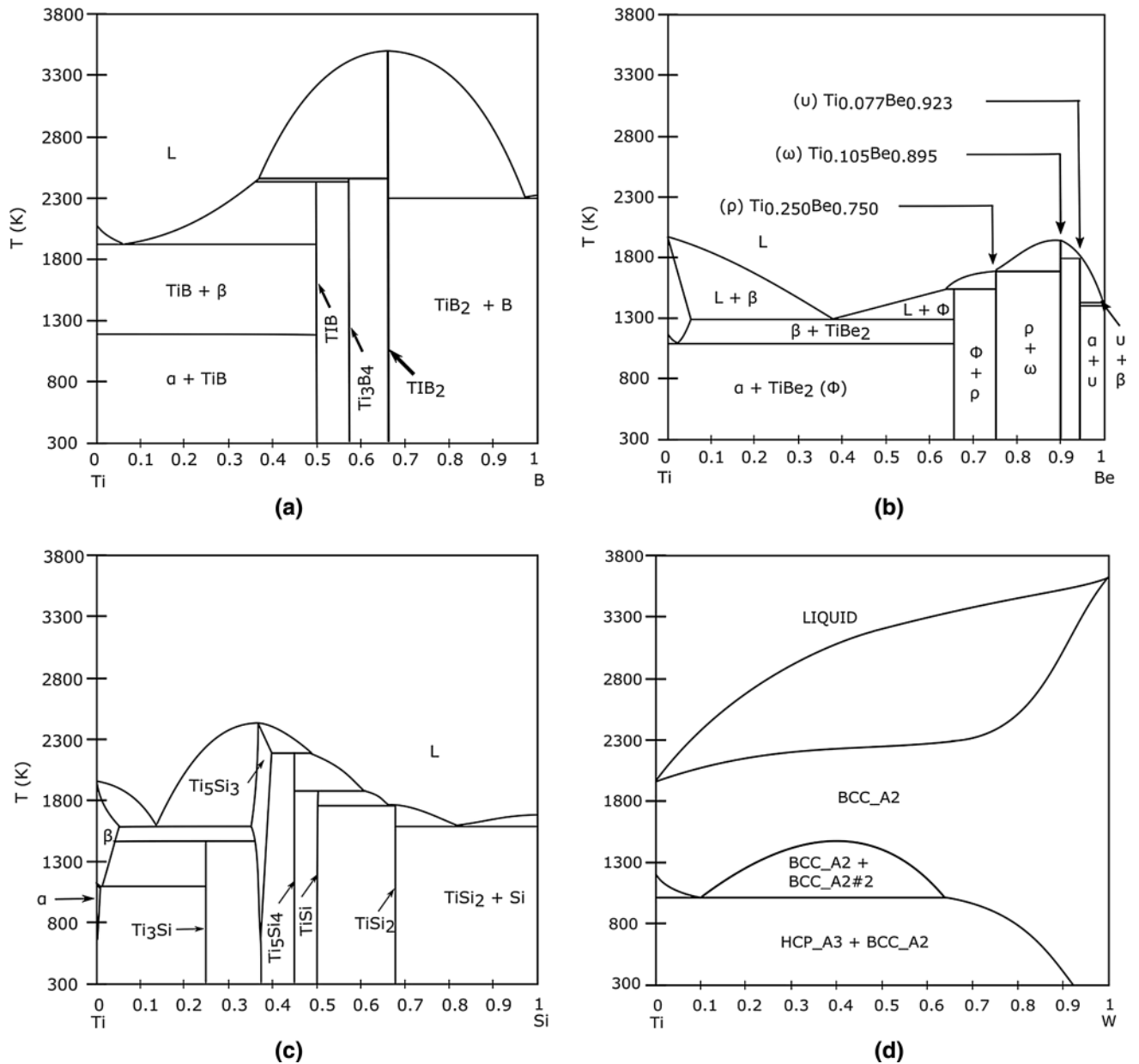These m, k, Q, and P are all 'average' values for phase diagrams, or as reported in the literature.

Fig. 1—Phase diagrams of (*a*) Ti-B (*b*) Ti-Be (*c*) Ti-Si (*d*) Ti-W.

preprogrammed incremental changes in the relative mass flow rate from powder feeders, and consequently, for the variation in the local composition along the length of the sample.

The second research activity used the fiber-optic laser to assess the influence of processing parameters on the microstructure. Specifically, in this second study the travel speed was changed between ~8.5 and ~12.5 mm/s to vary the energy density between 2.4 (~149) and 7.4 MJ/in^3 (~448 kJ/cm^3).[29] A total of 9 depositions were made with a range of energy densities. The geometry of these deposits right cylinders with a diameter of 7.62 mm and a height of 12.7 mm.

Following depositions, the deposits were sectioned from the substrate and cut in half longitudinally (*z* deposition direction). The specimen cross section was

then prepared for materials characterization using conventional metallographic techniques. The sections were ground using 240–800 grit wet/dry SiC abrasive papers followed by polishing using a 0.04 colloidal silica suspension. Following preparation, the specimen was cleaned using a solution sequence of acetone, water-surfactant mixture, water, and methanol. Imaging of the microstructure was carried out using a FEI™ Quanta 250 FE-SEM equipped with a field emission gun (FEG) source and a backscatter detector. The local compositions along the graded specimen were determined using standardless energy dispersive spectroscopy (EDS) and the values are reported to the nearest whole wt pct. Average grain size measurements following the Planimetric procedure[30] were conducted for further analysis and interpretation.

Table II. Parameters Used in the Simulation

Parameter	Value	Units
Substrate width	0.003	w_0 (m)
Substrate height	0.003	h_0 (m)
Emissivity	0.4	ε
Dynamic viscosity	4×10^{-3}	μ_0 (Pa s)
Laser beam radius	5×10^{-4}	r_0 (m)
Laser power	183–259–367	P (watts)
Thermocapillary coefficient	-2.7×10^{-4}	γ (N/m K)
Absorption*	15 pct	—
Liquidus temperature	1923 (1650)	T_L [K (°C)]
Density (liquid phase)	$5227.6 - 0.688*T$ (K)	ρ_l (Kg/m^3)
Density (solid phase)	$4462.6 - 0.1425*T$ (K)	ρ_s (Kg/m^3)
Thermal conductivity (liquid phase)	$-12.752 + 0.024*T$ (K)	λ (W/(m K))
Thermal conductivity (solid phase)	$3.5127 + 0.0127*T$ (K)	λ (W/(m K))
Specific heat capacity (liquid phase)	831	c_p (J/(Kg K))
Specific heat capacity (solid phase)	$412.7 + 0.1801*T$ (K)	c_p (J/(m K))

*Laser absorption based on experimental results from other authors.[43]

The 2D finite element model implements the conservation of energy, momentum and mass equations. The thermophysical properties (temperature dependent)[31,32] and parameters used in the calculations are summarized in Table II. The liquid phase region (assumed to be laminar flow and a Newtonian fluid) includes the Buoyancy and Marangoni effects. The set of equations are coupled and solved using the commercial package COMSOL Multiphysics®.

III. RESULTS AND DISCUSSION

A. As-Deposited Microstructure: Effect of W on Local Chemistry

In addition to the effect on the local chemistry when using elemental blends, it appears that tungsten has two additional effects. The first is that the so-called "fish-scale" patterns are typically tungsten rich. This is likely due to density differences in the liquid phase, even when the liquid is mostly homogeneous and well-mixed (see Figure 2(b)). The second can be observed in the series of figure insets in Figure 3(a), identified as *a-1*, *a-2*, and *a-3*. In addition to the macro-segregation, there are signatures of cellular or dendritic structures with a length scale of ~10 μm. All three of these sub-regions of Figure 3(a) has been enhanced so that this cellular/dendritic region is clear. Based upon the literature and the Comsol model describing the greatest gradient of temperature in the vertical (z) direction of deposition, it is reasonable to expect that the long direction of these dendrites is parallel to the ⟨001⟩β direction, as this cube direction is often associated with the maximum heat extraction rate during additive manufacturing. Figure 3(a-1) shows that the dendrites are growing parallel to the maximum heat gradient (as expected). In one portion of Figure 3(a), identified as *a-2*, it appears as if there are two different primary orientations of the dendrites, marked by two arrows. This difference is likely attributed to either one (or multiple) of the following possible effects. The first is

that the crystal orientations of two nucleating phases are both equally favorable, and both will grow until interrupted. The second is that the thermal gradients for this particular location of the melt pool are complex due to, for example, curved interfaces, and the eigenvectors of two adjacent locations point in different directions. Other possibilities include stabilization of particular growth directions from fluid flow. In the portion of Figure 3(a) identified as *a-3*, it appears as if the cellular/dendritic structure is being sectioned approximately normal to the growth direction, causing them to appear more circular than elongated.

As an important aside, owing to the differences in the vector motion during the deposition process, these various two-dimensional cross sections through the cellular/dendritic growth occur within a single micrograph. This suggests that it may be possible to extract 2D distributions of feature sizes/aspect ratios that may provide details of the three-dimensional microstructure without the need to conduct more expensive tomographic reconstructions of the material.

With respect to the compositional variations associated with the dendritic structure, Figures 4((a) through (d)) shows a series of micrographs taken at increasing magnifications, and culminating in Figure 4(d). The regions where composition is varying spatially are clear in Figures 4((c), (d)). In Figure 4((d), (e)), the line designates a compositional line profile obtained using energy dispersive spectroscopy. The solute variation ranged from ~5.5 to 6.5 wt pctW, and exhibited a periodic structure, as expected for a cellular or dendritic growth. In this particular region, the periodicity was ~7 μm. Importantly, there are multiple periods in this structure (~15 for this grain) even though the maximum heat gradient points toward the bottom of the molten pool, about 33 deg from vertical for this grain that is growing from a curved portion of the molten pool (observed in Figure 4(b)). This periodicity, as well as the truncated cellular structures shown in Figure 3((a), (a-3)), indicates that a Mullins and Sekerka instability[33,34] is operating with a characteristic wavelength of

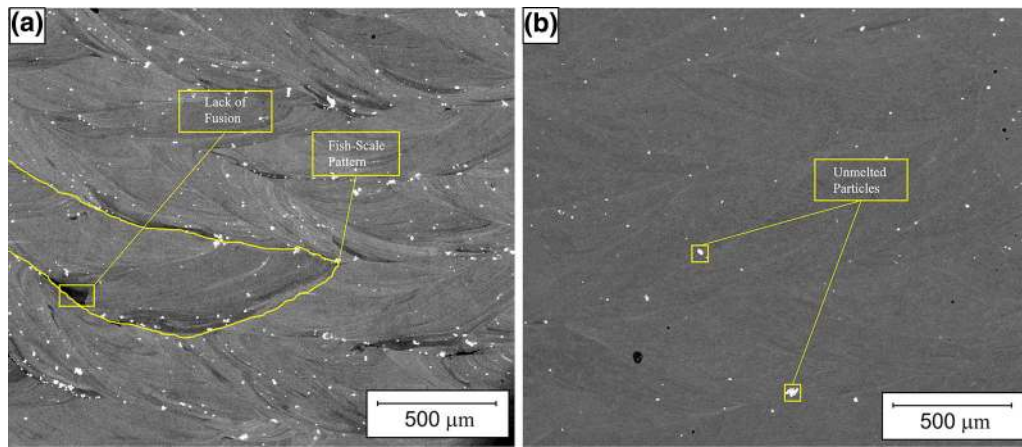Fig. 2—Backscattered electron micrographs for two deposited specimens (*a*) 2.4 MJ/in^3 (~149 kJ/cm^3) and (*b*) 7.4 MJ/in^3 (~448 kJ/cm^3).
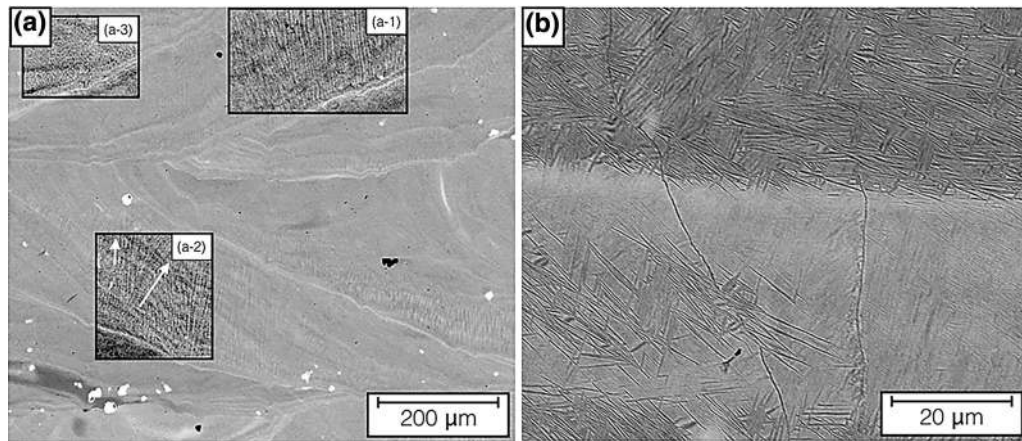

Fig. 3—Backscattered electron micrographs for a specimen deposited at 5.4 MJ/in^3 (~328 kJ/cm^3). (*a*) An lower magnification image showing the solute banding at the boundaries between successive laser passes and layers, with insets showing solute fluctuations due to solidification phenomena. (*b*) A higher magnification image showing the effect on solute banding on the resulting solid-state phase transformations, with regions of increased W stabilizing the *bcc β* phase and lower concentrations of W stabilizing the *hcp α* phase.

~7 *μ*m. Of note, the Mullins and Sekerka can be established by small perturbations in the solid-liquid interface, or in the thermal fields that arise from very localized turbulence at the solid/liquid interface. Once established, the perturbations become periodic in plane, and grow into either a cellular structure or a dendritic structure.

B. *Effect of W on Grain Size*

Figure 5((a) through (c)) illustrate backscattered electron micrographs taken along the graded specimen from the regions with the local average compositions of 5, 13, and 25 pctW, respectively. For all microstructures, the overall features are quite similar and consist of prior *β* grains and alpha laths within them. There are, as expected, variations in size and fraction of the *hcp α* and *bcc β* phases with the increasing tungsten content. When comparing the micrographs in Figure 5((a) through (c)), it can be seen that the increasing the tungsten concentration has resulted in the refinement of the *β* grain.

It is useful to present a brief review and analysis of previous results on grain refinement for the Ti-Si[24,25]

and Ti-B[17,18] systems to understand the applicability and interpretation of the Easton and St. John equation[13,22] for the Ti-W system results presented here. In their study, Bermingham *et al.* observed significant grain refinement of Ti (*i.e.*, average grain diameters dropping from 600 to 200 *μ*m) upon the addition of small quantities of Si (*i.e.* 0.05 to 0.9 wt pct).[24] They also compared their results with a similar study of Ti-Si system by Zhu *et al.*[25] which reports even greater grain refinement (up to 92 pct) with increase in Si content up to 2.75 wt pct. The Easton and St. John equation (grain size *d vs* the inverse of *Q*) for both studies is schematically shown in Figure 6 for such comparison. Importantly, the slope of the plot by Bermingham *et al.* is much lower than that of Zhu *et al.* which means that there is a difference in their results. Based upon Eq. [4] given in the introduction, the difference is related to the potency of nuclei (*b*), which is greater in the work of Bermingham. The *y*-intercept *a* is lower for the data by Zhu *et al.* indicating that the number of activated nuclei is higher. The conclusions drawn from this comparison by Bermingham *et al.*[24] were that the refinement for Zhu *et al.* plot comes from a high population of low
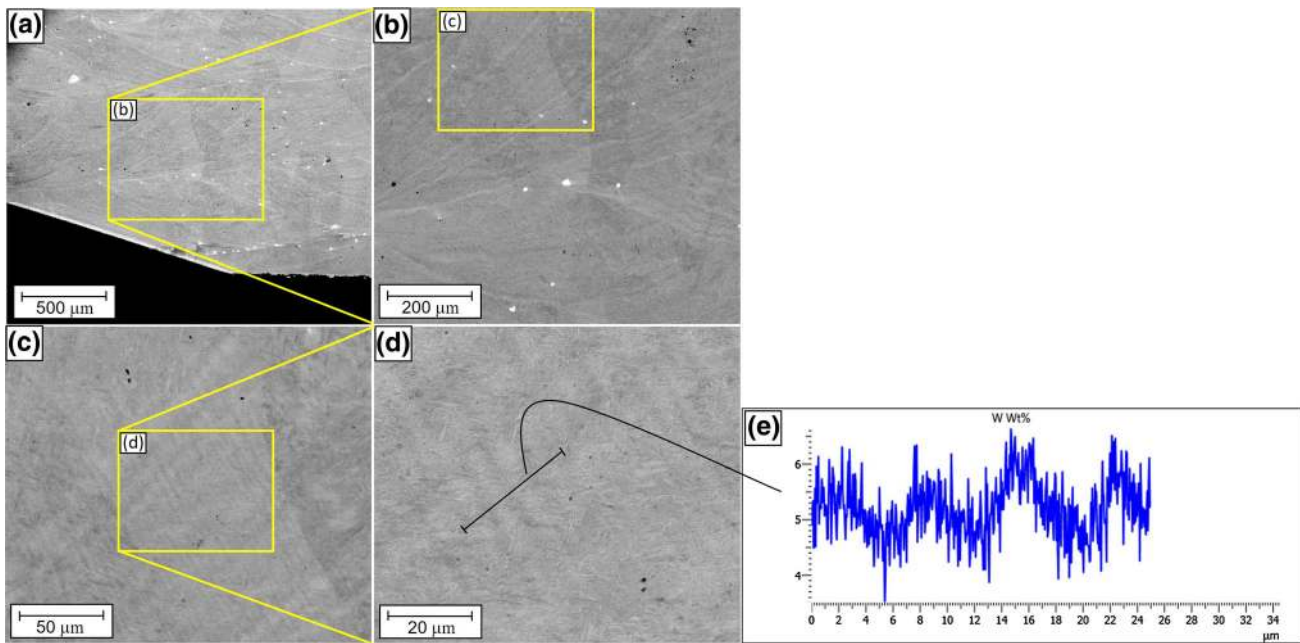
Fig. 4—Backscattered electron micrographs with the compositional variations (at energy density of 7.4 MJ/in^3) (~448 kJ/cm^3) measured using energy dispersive spectroscopy. (*a* through *d*) Backscattered electron micrographs showing increasing magnification of the same region, illustrating the relation between the boundaries between successive laser passes (a, b) to grains (b, c) to solute partitioned regions in the cellular structure. (*e*) Compositional profile collected using energy dispersive spectroscopy corresponding to the line identified in (d).
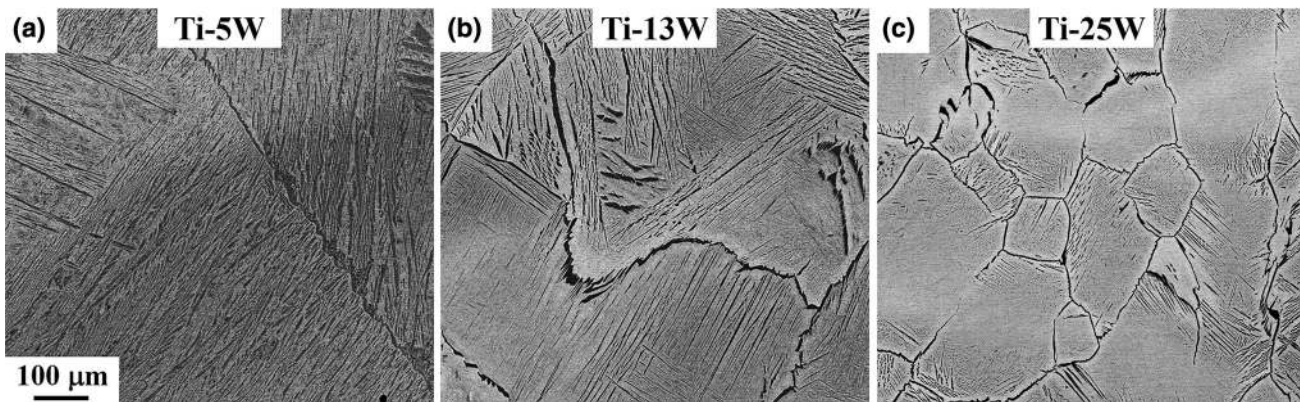
Fig. 5—Backscattered SEM micrographs corresponding to the local average compositions of (*a*) Ti-5W, (*b*) Ti-13W, (*c*) Ti-25W.

potency nuclei and the refinement for their study comes from a low population of high potency nuclei. However, Bermingham *et al*.[24] did not explain the reason for difference in the *b* term or the slope of the curves (see Eq. [5]), calculated for the same system, Ti-Si. The observed differences in the slopes for the same system in Figure 6 can be interpreted by considering the proportionality between the undercooling factor expressed as $P = 62C_0$ (Ti-Si system) and the *b* term of the Easton and St. John equation. The results presented by Zhu *et al*. had a greater silicon content range than Bermingham *et al*., increasing the attending undercooling factor while reducing the potency of nuclei.

The interpretation of the slope is important because it allows for a preliminary prediction of the *b* term based on the undercooling factor of the specific binary system

of interest. The fact that the trend of the data was concordant with straight lines also indicates that the nuclei population is relatively constant for both cases. While the origin of nuclei was unclear for both cases, Bermingham *et al*. did not observe any silicide compounds in the microstructure and the Ti-Si phase diagram does not show any intermetallic to be present in the liquid before the primary solidification.[24] On the other hand, Zhu *et al*. reported evidence for the presence of titanium silicide, Ti_5Si_3, after 1.33 wt pct Si additions, but those were present after the primary solidification. Therefore, Bermingham *et al*. argued that the nuclei origin for both cases could come from impurities in the base material or impurities from the silicon additions, an argument that is rational considering the potency of titanium to getter various interstitial

elements, including oxygen, that may stabilize Ti-Si complexes.

These two different results for the same system are a clear indication that a better understanding of the nuclei present in the base material is required to make a good prediction of grain refinement in titanium alloys *via* the addition of solutes.[24] In a subsequent study performed by Bermingham *et al.*[18] they discussed the refinement of titanium alloys by boron additions and applied the previous model that takes into account the nuclei effect that was ignored in the Ti-B study made by Tamirisakandala *et al.*[17] Considering that the nuclei effect should be always taken into account, Bermingham *et al.* found that the addition of boron is not introducing a significant amount of nuclei, so the refining mechanism in this specific case is mainly governed by solute additions and this results confirms the initial assumptions made by Tamirisakandala *et al.*[18]
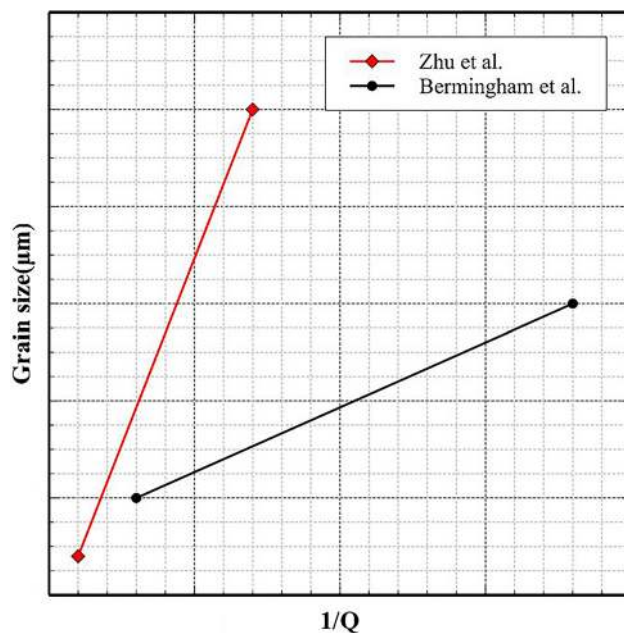

Fig. 6—Schematized plots for Zhu *et al.* and Bermingham *et al.* results, showing the grain refinement as a function of the reciprocal of the grain restriction factor in Ti-Si system.

In a more generic analysis of titanium alloys refined by solute additions, performed by Bermingham *et al.*, two possible scenarios are posed to explain the grain refinement.[11] The first scenario is a solute-based mechanism where the grain refinement is increasing with solute content until reaching a saturation point that depends upon a preestablished nuclei population available (see Figure 7(a)). On the other hand, the second scenario is a nuclei-based mechanism where the solute addition is creating more nuclei for new grains that increases the grain refinement without the previous saturation point (see Figure 7(b)).[11] Figures 7((a), (b)) show the schematic interpretation of these two different mechanisms and the analysis of the present research work on refining titanium alloys *via* tungsten additions is evaluated under these two possible scenarios.

Applying these concepts regarding the operation of two different possible mechanisms that potentially explain the grain-refinement mechanism in Ti-W system, the Q factor should be calculated and the corresponding Easton and St. John curve should be plotted. The expected Easton and St. John curve for Ti-W system with an undercooling factor expressed as $P = 11.2C_0$, and tungsten additions that increase the nuclei population, is a curve with a high slope and a y-intercept that decreases with increasing concentration of tungsten. The variation in the grain size as a function of tungsten concentration is plotted in Figure 8(a). When comparing Figure 8(a) with Figure 7((a), (b)) it can be seen that the most probable grain refinement scenario for Ti-W system is the second scenario, *i.e.* nuclei-based mechanism (see Figure 7(b)). However, this scenario applies for cases where the contribution from the solute mechanism is minimal in other words where the Q factor is very small (*e.g.*, for Al and V which are common alloying elements in Ti). In contrast, tungsten has a significant Q factor of about $22.65C_0$. Despite the high Q factor, the scenario (b) still fits well for Ti-W system.

At low concentrations of tungsten in Ti, the liquidus slope is higher than for other compositions that provides an even higher Q factor and signifies the solute effect. However, a Q factor of about $22.65C_0$ is a reasonable average value (indeed, and importantly, it is *very* close to the Q value for Si). Figure 8(b) shows the application of the Easton and St. John[22] equation for Ti-W system.
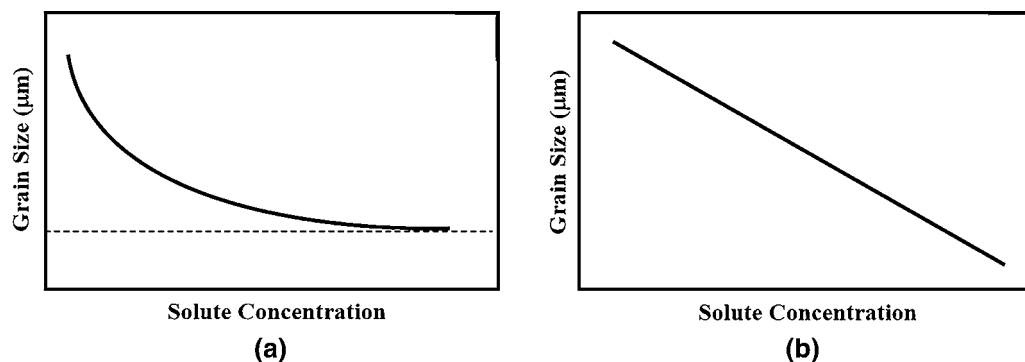

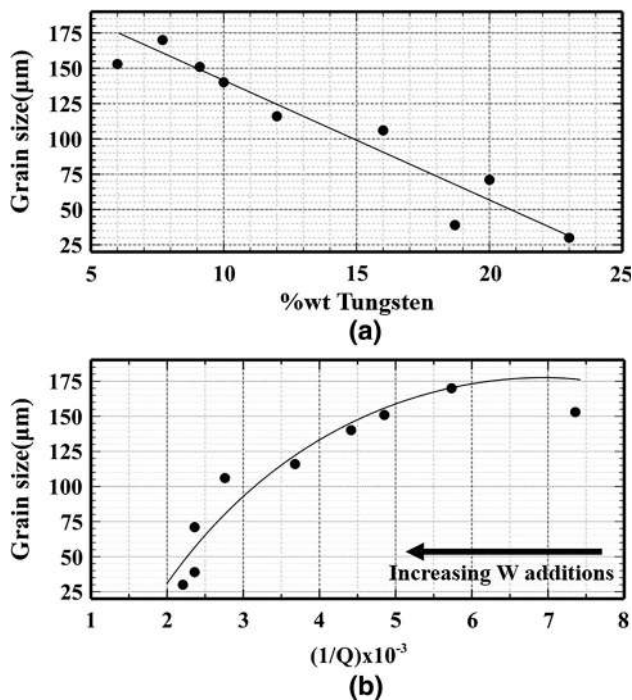Fig. 7—Schematic representation of (*a*) first scenario and (*b*) second scenario.

Fig. 8—Plots of (a) grain size as a function of W concentration and (b) grain size as a function of the reciprocal of the grain restriction factor using Easton and St. John model.

It can be observed that the b term is as expected by the Easton and St. John model with a high slope across the composition range, indicating low potency of nuclei by the high Q factor of Ti-W system. In fact, when the data of Bermingham *et al.* (Figure 6) are compared with Figure 8(b), it is clear that the data for W would lie on the extension of the line for Bermingham *et al.*'s Ti-Si work. Additionally, a continuous decay in the curve is observed inasmuch the W content is increasing (lower $1/Q$) which means that the y-intercept parameter *a* is following the expected behavior when the population of nuclei is increasing with the solute additions. The common presence of unmelted W particles observed within Ti-W samples as in the SEM micrograph (see Figure 2(a)) is responsible for increase in the nuclei population.

C. *As-Deposited Microstructure: Unmelted Powder Particles and Porosity*

Backscattered electron micrographs showing large fields of views in the *xz* plane for the highest- and lowest-energy-density-deposited specimens (fixed composition) are shown in Figures 2((a), (b)) for 2.4 (~149) and 7.4 MJ/in^3 (~448 kJ/cm^3), respectively.* Not surprisingly,

---

*Throughout the remainder of the paper, mixed units will be intentionally used for energy densities. The first units correspond to the mixed units that result from the instrument variables, and the second set of units correspond to SI units.

the higher power density corresponds with a larger degree of compositional homogeneity at a macrolevel. There are fewer unmelted W particles in Figure 2(b) than that in Figure 2(a). The relationship between unmelted particles and energy density is shown in Figure 3. In addition, the as-deposited microstructure corresponding to the lower energy-density level contains multiple lack of fusion regions of varying sizes, some as large as 250 μm in length. In addition to these lack of fusion regions, there are other types of pores in both micrographs, although it should be noted that it is difficult to assess the origin of porosity in AM material, especially when elemental powder blends are used. In some cases, these pores which appear in metallographic specimens can be attributed to 'unmelted' powder particles that have been pulled out of the material during polishing.

These results parallel earlier results[8] where elemental powder blends were used to produce Ti-based alloys using additive manufacturing. In these studies, it was observed that the enthalpy of mixing had a pronounced effect on the homogeneity of the microstructure. While there are other thermodynamic variables that must be considered, including the enthalpy of fusion of the elements, the reflectivity of the elements, and the specific heat capacity of the elements, previous work has shown the importance of the enthalpy of mixing. It is most likely that the enthalpy of mixing of the liquids provides a heat source *within the molten pool*, providing a localized temperature gradient and promoting Bénard–Marangoni mass transfer. When comparing the Ti-6W pctwt results here, they require more far energy than other binary titanium alloys alloyed with either Cr or Mo,[35] although the enthalpy of fusion and specific heat capacity are within ~10 pct of the values of the previous work. This provides additional evidence regarding the importance of the enthalpy of mixing as a key variable at compositional homogeneity when using elemental powder blends.

It is also clear that compositional fluctuations exist over large length scales. The contrast in the backscattered electron micrographs shown in Figures 2((a) and (b)) are proportional to the average atomic mass. Thus, the brighter regions correspond to regions that are more tungsten rich, while the darker gray regions correspond to regions that are tungsten lean. These features are clear in Figure 2(a), as well as near the bottom left of Figure 3(a), which was acquired from a fixed composition specimen deposited at 5.4 MJ/in^3 (~328 kJ/cm^3). The darker (Ti-rich) regions (*see* Figures 2(a) and 3(a)) tend to be near the bottom of the molten pools and near W particle clusters, which may be due to the combination of lower superheats and local heat extraction of the W particles, which require additional energy to reach their melting points and then melt (see the effect of energy density on unmelted particles, Figure 9). In addition to these darker features, there are brighter bands, corresponding to tungsten-rich regions. Figure 3(b) shows that this compositional fluctuation will have a pronounced effect on the subsequent phase transformations, as the tungsten rich region has a lower fraction of *hcp* α-laths than the tungsten lean regions.

This is as expected, as tungsten is considered to be a *bcc* β-stabilizing element in titanium alloys.

In both the tungsten lean and tungsten rich regions, it is clear that there was liquid metal flow, pulling either tungsten lean or tungsten rich regions into the molten pool. These bands have characteristic shapes to them. The velocity of liquid in a molten pool can be simulated using COMSOL multiphysics® software and including the effects of buoyancy and the Bérnard-Marangoni mass transfer due to temperature effects.[31,36] The results of these simulations, even without the complications of elemental powder particles, are shown in Figure 10. These results (for two different energy densities and time steps) show that the dominant flow pattern is along the to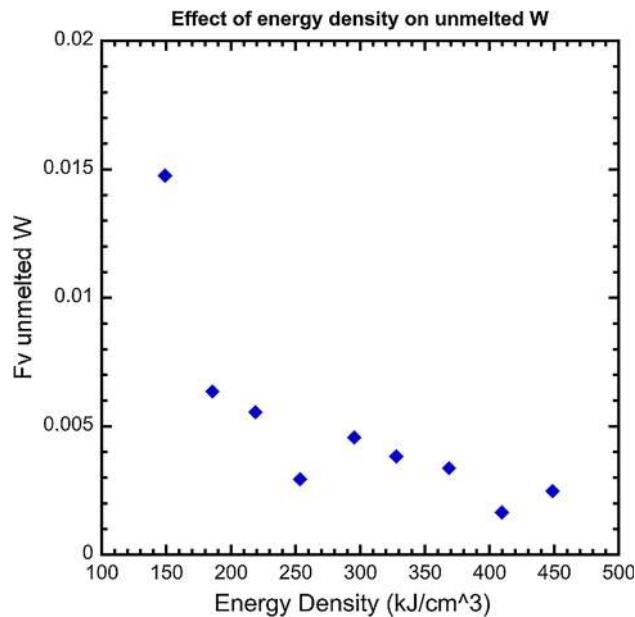p of the molten pool, down into the molten pool at a certain fraction between the edge and the center, and then along the bottom of the molten pool back up to the surface. This temperature driven mass transport explains the macro-solute patterns observed in elemental powder blends, as shown in Figures 2(a) and 3(a).
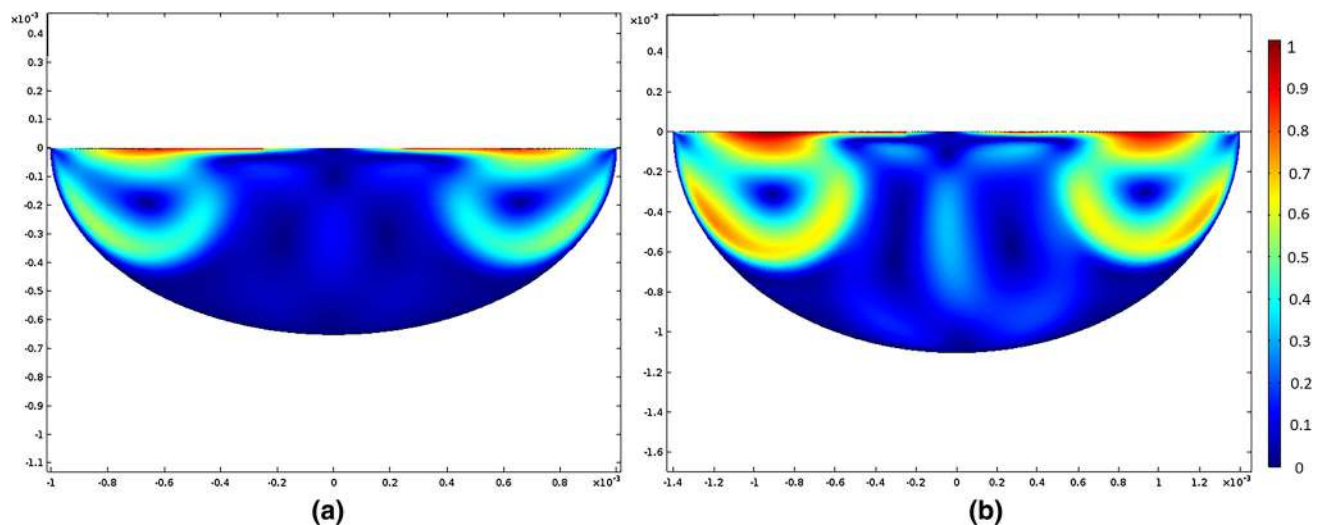
D. *Effect of Power on Grain Size*

To assess the effect of power on grain size, two approaches were adopted. The first approach is to plot the experimentally measured results against an energy-density term (ρ_{energy}**) that integrates the inci-

---

**Energy density may be defined in the following way: $\rho_{energy} = \frac{P}{v \cdot t_{layer\ spacing} \cdot t_{hatch\ width}}$ where P is the laser power, v is the velocity of the laser, $t_{layer\ spacing}$ is the layer spacing, and $t_{hatch\ width}$ is the distance between passes. Both layer spacing and hatch width provide information regarding the radial distribution of temperature.

---

dent power, travel speed, and hatch width. These terms represent equivalencies to terms used in the Rosenthal equations of a moving heat-source, with an additional term to capture the area over which the power is distributed. This term has been shown to be related to properties and defects in the past[37,38] and is a reasonable initial variable against which to compare the resultant grain size of the material. The grain size is the average of *minimum* grain diameters from the epitaxial grains, and is thus an x' (or y, or xy, as this coordinate is ill defined) vector measurement recorded from an image of the (x',z) plane. The influence of energy density on the resulting grain size is shown in Figure 11(a). Not surprisingly, as the energy density increases, the grain size also increases.

To understand the reason why the grain size increases with the increasing power, COMSOL multiphysics simulations were conducted using the experimental variables to quantify the cooling rates associated with the different input energy densities. These calculations
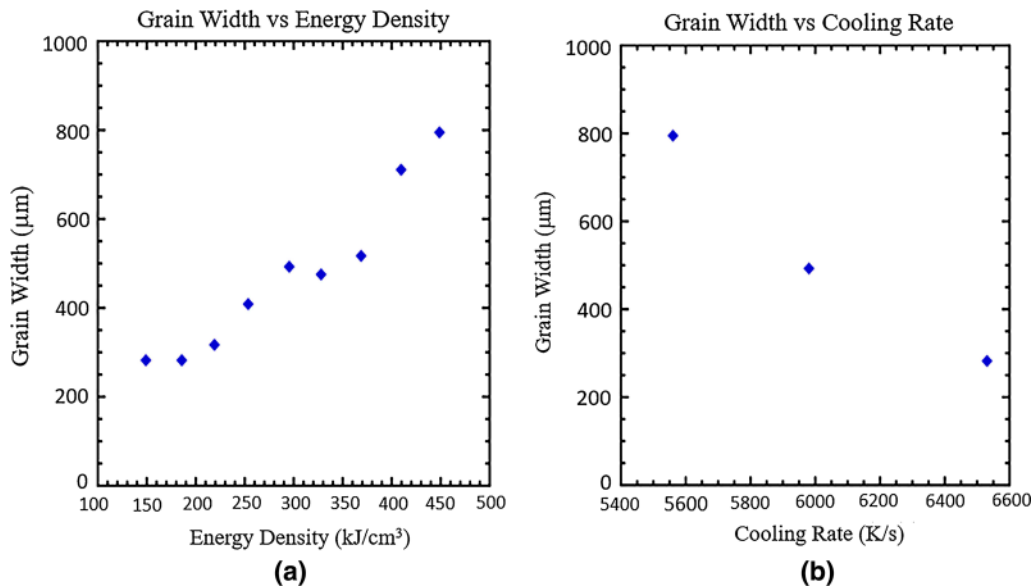
Fig. 9—Fraction of unmelted particles as a function of energy density.

Fig. 10—Fluid flow velocity (m/s) in a molten pool (*a*) 183 W and (*b*) 367 W.

Fig. 11—Grain sizes as a function of (*a*) energy density and (*b*) cooling rate.

were performed for energy densities of 2.4 (~149), 4.2 (~257), and 7.4 MJ/in^3 (~449 kJ/cm^3), respectively. The resulting cooling rates were 6530 K/s, 5980 K/s, and 5560 K/s (6257 °C/s, 5707 °C/s, and 5287 °C/s), respectively. These calculated cooling rates are in good agreement with the specific range of 10^3 to 10^4 K/s for rapid solidification in LENS™ process reported by Zheng *et al.* from experimental[39] and computational results.[40,41] The corresponding average *minimum* grain size was plotted against these three calculated cooling rates, and the results are shown in Figure 11(b). There is a very clear relationship between the cooling rate and the grain size, which is expected.

Depending upon the modeling strategy that is used, grain size can exhibit an inverse relationship (arising from $d = \mu f \frac{\Delta T_N^2}{\dot{T}}$, where μ is the interface mobility, f is the fraction nuclei, ΔT_N is the undercooling, and $\dot{T}$ is the cooling rate,[42] assuming a relatively constant undercooling), or a relationship closer to $d = a t_f^n = b(G \cdot R)^{-n}$, where a and b are material constants, t_f is the solidification time, and G and R take their traditional definitions of the thermal gradient and growth rate, respectively. In this second approach, the exponent n typically ranges from $1/3$ to $1/2$ when d is used to assess dendrite arm spacing. Given the limited data in this figure, it is not reasonable to fit a curve to the data. Nonetheless, the inverse nature of the relationship is clear.

IV. CONCLUSIONS

A compositionally graded Ti-xW specimen ($0 \leq x \leq 30$ wt pct) was produced to study the grain-refinement effect of tungsten and the associated mechanisms in Ti-based alloys. A significant reduction in the grain size was observed from >170 to ~30 μm with addition of up to 23 wt pct W. To understand the operating mechanisms of grain refinement, the Easton and St. John model was applied which fitted well for Ti-W system. A comparison of previous results from other researchers provided the understanding to predict the tendency of the curve and then separate the concepts of the solute-based mechanism and the nuclei-based mechanism to reduce the grain size. The Ti-W system did not show any indication of grain-refinement saturation point in the studied compositional range. The nuclei population is increasing with the solute addition, and the significant Q factor of $22.65C_0$ is consistent with the second scenario, but with a considerable solute effect. Therefore, the Easton and St. John model is a good method to analyze and interpret the grain-size refinement in Ti-based alloys.

The relationship between energy density and grain size from the nine specimens revealed the tendency to increase the prior beta grain size inasmuch as energy density is augmented. The more the absorbed energy the greater is the size of the molten pool, which in turn implicates lower cooling rates. The decreasing cooling rates calculated using the COMSOL Multiphysics® simulation are concordant with the increasing prior beta grain size across the studied energy-density range.

Non-Ferrous Structural Alloys (CANFSA), an NSF Industry/University Cooperative Research Center (I/UCRC) between the Iowa State University and the Colorado School of Mines. This article is intended to appear as one of two companion articles. This article focuses on the experimental methods associated with additive manufacturing of Ti-xW specimens, and the companion article by Rolchigo et al. is focused on the simulation of solidification associated with additive manufacturing.

OPEN ACCESS

REFERENCES

1. N. Hrabe and T. Quinn: *Mater. Sci. Eng. A*, 2013, vol. 573, pp. 264–70.
2. N. Hrabe and T. Quinn: *Mater. Sci. Eng. A*, 2013, vol. 573, pp. 271–77.
3. Y.-J. Liang, X.-J. Tian, Y.-Y. Zhu, J. Li, and H.-M. Wang: *Mater. Sci. Eng. A*, 2014, vol. 599, pp. 242–46.
4. F. Wang, S. Williams, P. Colegrove, and A.A. Antonysamy: *Metall. Mater. Trans. A*, 2012, vol. 44A, pp. 968–77.
5. L.E. Murr, S.M. Gaytan, A. Ceylan, E. Martinez, J.L. Martinez, D.H. Hernandez, B.I. Machado, D.A. Ramirez, F. Medina, and S. Collins: *Acta Mater.*, 2010, vol. 58, pp. 1887–94.
6. L. Thijs, F. Verhaeghe, T. Craeghs, J.V. Humbeeck, and J.-P. Kruth: *Acta Mater.*, 2010, vol. 58, pp. 3303–12.
7. G. Bi, C.-N. Sun, H.-C. Chen, F.L. Ng, and C.C.K. Ma: *Mater. Des.*, 2014, vol. 60, pp. 401–08.
8. K.I. Schwendner, R. Banerjee, P.C. Collins, C.A. Brice, and H.L. Fraser: *Scr. Mater.*, 2001, vol. 45, pp. 1123–29.
9. P. Samimi, Y. Liu, I. Ghamarian, D.A. Brice, and P.C. Collins: *Corros. Sci.*, 2015, vol. 97, pp. 150–60.
10. K. Kunze, T. Etter, J. Grässlin, and V. Shklover: *Mater. Sci. Eng. A*, 2015, vol. 620, pp. 213–22.
11. M.J. Bermingham, S.D. McDonald, M.S. Dargusch, and D.H. StJohn: *J. Mater. Res.*, 2008, vol. 23, pp. 97–104.
12. M.J. Bermingham, S.D. McDonald, D.H. StJohn, and M.S. Dargusch: *J. Alloys Compd.*, 2009, vol. 481, pp. L20–23.
13. M.A. Easton and D.H. StJohn: *Acta Mater*, 2001, vol. 49, pp. 1867–78.
14. D.H. StJohn, A. Prasad, M.A. Easton, and M. Qian: *Metall. Mater. Trans. A*, 2015, vol. 46A, pp. 4868–85.
15. K.V. Wong and A. Hernandez: *ISRN Mech. Eng.*, 2012, vol. 2012, pp. 1–10.
16. M. Easton and D. St: *John: Essential Readings in Light Metals*, Springer, Queensland, 2016, pp. 393–99.
17. S. Tamirisakandala, R.B. Bhat, J.S. Tiley, and D.B. Miracle: *Scr. Mater.*, 2005, vol. 53, pp. 1421–26.
18. M.J. Bermingham, S.D. McDonald, K. Nogita, and D.H. St: John and M. S. Dargusch.*Scr. Mater.*, 2008, vol. 59, pp. 538–41.
19. P.C. Collins, D.A. Brice, P. Samimi, I. Ghamarian, and H.L. Fraser: *Annu. Rev. Mater. Res.*, 2016, vol. 46, pp. 63–91.
20. R. Banerjee, S. Nag, S. Samuel, and H.L. Fraser: *J. Biomed. Mater. Res. A*, 2006, vol. 78, pp. 298–305.
21. S. Nag, S. Samuel, A. Puthucode, and R. Banerjee: *Mater. Charact.*, 2009, vol. 60, pp. 106–13.
22. M.A. Easton and D.H. St John: *Metall. Mater. Trans. A*, 2005, vol. 36A, pp. 1911–20.
23. D.H. St John, M. Qian, M.A. Easton, P. Cao, and Z. Hildebrand: *Metall. Mater. Trans. A*, 2005, vol. 36A, pp. 1669–79.
24. M.J. Bermingham, S.D. McDonald, M.S. Dargusch, and D.H. St John: *Scr. Mater.*, 2008, vol. 58, pp. 1050–53.
25. J. Zhu, A. Kamiya, T. Yamada, A. Watazu, W. Shi, and K. Naganuma: *Mater. Trans.*, 2001, vol. 42, pp. 336–41.
26. J. Zhu, A. Kamiya, T. Yamada, W. Shi, and K. Naganuma: *Mater. Sci. Eng. A*, 2003, vol. 339, pp. 53–62.
27. S.X. Liang, X.J. Feng, L.X. Yin, X.Y. Liu, M.Z. Ma, and R.P. Liu: *Mater. Sci. Eng. C. Mater. Biol. Appl.*, 2016, vol. 61, pp. 338–43.
28. T. Quested, A. Dinsdale, and A. Greer: *Acta Mater.*, 2005, vol. 53, pp. 1323–34.
29. B. Vandenbroucke and J.-P. Kruth: *Rapid Prototyp. J.*, 2007, vol. 13, pp. 196–203.
30. ASTM International: *E112-13, Annual Book of ASTM Standards*, ASTM International, West Conshohocken, PA.
31. S. Morville, M. Carin, P. Peyre, M. Gharbi, D. Carron, P. Le Masson, and R. Fabbro: *J. Laser Appl.*, 2012, vol. 24, pp. 1–9.
32. M. Boivineau, C. Cagran, D. Doytier, V. Eyraud, M.H. Nadal, B. Wilthan, and G. Pottlacher: *Int. J. Thermophys.*, 2006, vol. 27, pp. 507–29.
33. W.W. Mullins and R.F. Sekerka: *J. Appl. Phys.*, 1963, vol. 34, p. 323.
34. W.W. Mullins and R.F. Sekerka: *J. Appl. Phys.*, 1964, vol. 35, p. 444.
35. P.C. Collins, R. Banerjee, and H.L. Fraser: *Scripta Mater.*, 2003, vol. 48, pp. 1445–50.
36. M.A. Moncayo, S. Santhanakrishnan, H.D. Vora, and N.B. Dahotre: *Opt. Laser Technol.*, 2013, vol. 48, pp. 570–79.
37. N. Klingbeil, S. Bontha, C. Brown, D. Gaddam, P. Kobryn, H. Fraser, and J. Sears: Report No. ADP020465, DTIC Austin, Texas, August 4 2004.
38. J.W. Sears: Report No. LM-02K021, Lockheed Martin Corporation, Schenectady, NY, April 5, 2002.
39. B. Zheng, Y. Zhou, J.E. Smugeresky, J.M. Schoenung, and E.J. Lavernia: *Metall. Mater. Trans. A*, 2008, vol. 39, pp. 2237–45.
40. W.E. Frazier: *J. Mater. Eng. Perform.*, 2014, vol. 23, pp. 1917–28.
41. B. Zheng, Y. Zhou, J.E. Smugeresky, J.M. Schoenung, and E.J. Lavernia: *Metall. Mater. Trans. A*, 2008, vol. 39A, pp. 2228–36.
42. P.R. Sahm, H. Jones, and C. Adam: *Science and Technology of the Undercooled Melt: Rapid Solidification Materials and Technologies.* Illustrated ed., Springer, Netherlands, 2012, pp. 166–78.
43. P. Peyre, P. Aubry, R. Fabbro, R. Neveu, and A. Longuet: *J. Phys. D*, 2008, vol. 41, p. 025403.